Final Report on AOARD-11-4050

Metal/dielectric multilayers for high resolution imaging

By Dao Hua ZHANG, NTU

Summary

The project is conducted from 1 July 2011 to 30 June 2012. In this period of time, we have carried out research on metal, dielectric and multilayer structures theoretically and experimentally. The Main achievements include the follows:

- We designed and simulated metal-dielectric structures for beam splitting with subwavelength resolution.
- We designed, simulated, fabricated and characterized binary zone plate plasmonic lens for super focusing. The full width at half maximum of the focus point achieved is about 300 nm for the incidence of 632 nm.
- We developed low-loss on-chip integrated plasmonic waveguide based on simple fabrication steps on silicon-on-insulator platform and achieved a record low loss, to the best of our knowledge.
- We proposed novel dielectric nanocavity metamaterial lens which is expected to have longer transmission distance, higher resolution and capable of magnification with proper design.

List of publications from this project

- Yueke Wang, Dao Hua Zhang*, Jun Wang, Ming Yang, Dongdong Li and Zhengji Xu, "Beam splitting with subwavelength resolution using combined metallodielectric films" Journal of Optics, J. Opt. 14 015103, 2012.

- Jun Wang[1], Dao Hua Zhang[1,*], Fei Qin[1], Qian Wang[1], Dongdong Li[1], Yueke Wang[1], Zhengji Xu[1] and Jinghua Teng[2], "A binary zone plate plasmonic lens based on a dipole field", to be published.

- Landobasa Y. M. Tobing, Liliana Tjahjana, and Dao Hua Zhang, "Demonstration of low-loss on-chip integrated plasmonic waveguide based on simple fabrication steps on silicon-on-insulator platform", submitted to Applied Physics Letters.

- Dongdong Li,[1] Dao Hua Zhang,[1,a)] Changchun Yan,[2] Yueke Wang, "Dielectric nanocavity metamaterial lens for super resolution imaging in visible range", To be published.

Report Documentation Page		*Form Approved* *OMB No. 0704-0188*

Public reporting burden for the collection of information is estimated to average 1 hour per response, including the time for reviewing instructions, searching existing data sources, gathering and maintaining the data needed, and completing and reviewing the collection of information. Send comments regarding this burden estimate or any other aspect of this collection of information, including suggestions for reducing this burden, to Washington Headquarters Services, Directorate for Information Operations and Reports, 1215 Jefferson Davis Highway, Suite 1204, Arlington VA 22202-4302. Respondents should be aware that notwithstanding any other provision of law, no person shall be subject to a penalty for failing to comply with a collection of information if it does not display a currently valid OMB control number.

1. REPORT DATE **07 AUG 2012**	2. REPORT TYPE **Final**	3. DATES COVERED **01-07-2011 to 30-06-2012**
4. TITLE AND SUBTITLE **Characterization of metal/dielectric multilayers with in-situ ellipsometry**		5a. CONTRACT NUMBER **FA23861114050**
		5b. GRANT NUMBER
		5c. PROGRAM ELEMENT NUMBER
6. AUTHOR(S) **Dao Hua Zhang**		5d. PROJECT NUMBER
		5e. TASK NUMBER
		5f. WORK UNIT NUMBER
7. PERFORMING ORGANIZATION NAME(S) AND ADDRESS(ES) **Nanyang Technological University,Nanyang Avenue,639798,Singapore,SG,639798**		8. PERFORMING ORGANIZATION REPORT NUMBER **N/A**
9. SPONSORING/MONITORING AGENCY NAME(S) AND ADDRESS(ES) **AOARD, UNIT 45002, APO, AP, 96338-5002**		10. SPONSOR/MONITOR'S ACRONYM(S) **AOARD**
		11. SPONSOR/MONITOR'S REPORT NUMBER(S) **AOARD-114050**
12. DISTRIBUTION/AVAILABILITY STATEMENT **Approved for public release; distribution unlimited**		
13. SUPPLEMENTARY NOTES		
14. ABSTRACT **The primary objective of the project is to explore new metals and dielectrics suitable for metamaterials in the visible frequency range and investigate their properties of the multilayer structures for high resolution imaging application. This project aims to investigate metal-dielectric structures by simulation and experiment and explore their applications for super-resolution imaging and nanophotonics as they have great potential for real-time in situ observation of complex molecular machinery in living biological cells and new generation photonic technology.**		
15. SUBJECT TERMS **meta materials, Materials Characterization**		

16. SECURITY CLASSIFICATION OF:			17. LIMITATION OF ABSTRACT	18. NUMBER OF PAGES	19a. NAME OF RESPONSIBLE PERSON
a. REPORT **unclassified**	b. ABSTRACT **unclassified**	c. THIS PAGE **unclassified**	**Same as Report (SAR)**	**12**	

Standard Form 298 (Rev. 8-98)
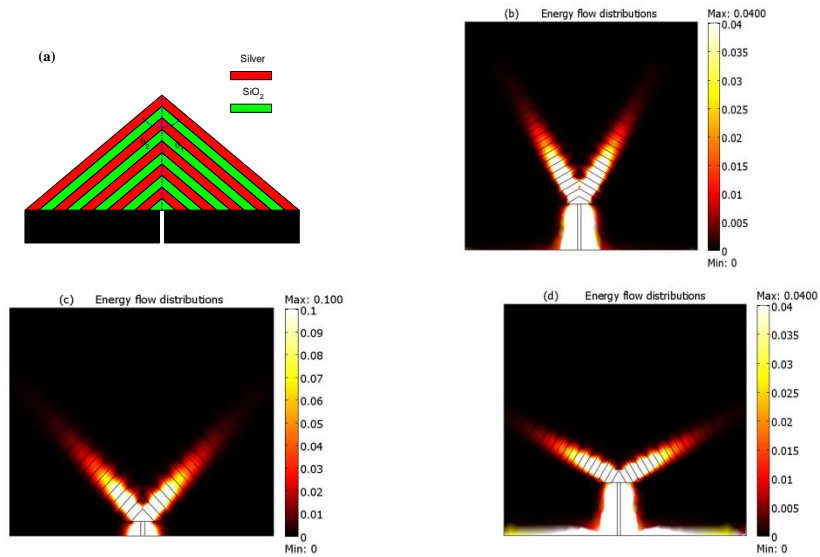Prescribed by ANSI Std Z39-18

1. Introduction

Metamaterials have many potential novel applications, such as cloaking, imaging and novel photonic devices [1-7]. This project aims to investigate metal-dielectric structures by simulation and experiment and explore their applications for super-resolution imaging and nanophotonics as they have great potential for real-time in situ observation of complex molecular machinery in living biological cells and new generation photonic technology. This report briefly presents the work carried out in the project.

2. Results

2.1 Metal-dielectric structures for beam splitting with subwavelength resolution

We propose a set of metamaterials composed of the combined metallodielectric films. The energy flow distributions of the structures are investigated by using the Finite Element Method (FEM). It is found that the beams split and propagate along the normal direction to the films. After propagating to the far field (about one wavelength), the resolution of the beams are still below half wavelength. Two beams splitting with uniform intensities or non-uniform intensities, multi-beams splitting, and reflected-beams splitting are obtained by changing the structures. The numerical results show a method for designing the subwavelength beam splitters.

Fig 1(a) shows the structure of the two beams splitter. When $\theta_1 = \theta_2 = \theta$, the structure can be used as a two uniform beams splitter. Energy flow distributions are simulated and shown in Figs 1(b)-(d) for $\theta = \pi/3$, $\pi/4$, $\pi/6$ and $\pi/12$, and the splitter angles are $\pi/6$, $\pi/2$, $\pi/3$ and $5\pi/12$, respectively. After the split beams propagate 380nm (more than one wavelength) along the normal direction to the film, the full width at half maximum (FWHM) of the beams is still below half wavelength. In Fig 1(f), the cross-section views of the output power along one of the two outer surfaces are plotted, and the FWHMs are about 56 nm, 52 nm, 54 nm and 54nm for $\theta = \pi/3$, $\pi/4$, $\pi/6$ and $\pi/12$, respectively. The center to center distances between two split beams are about 380nm, 540nm, 660nm, and 735nm. So this set of structures provides a method to produce and split two subwavelength uniform beams with various split angles.
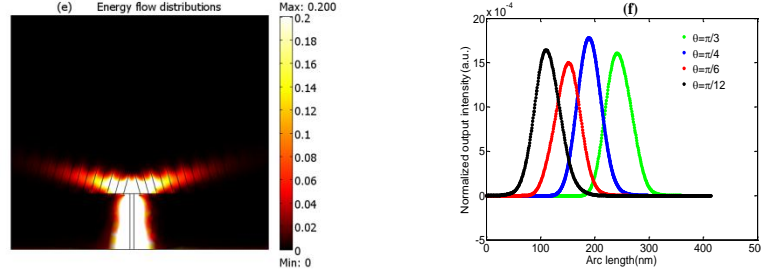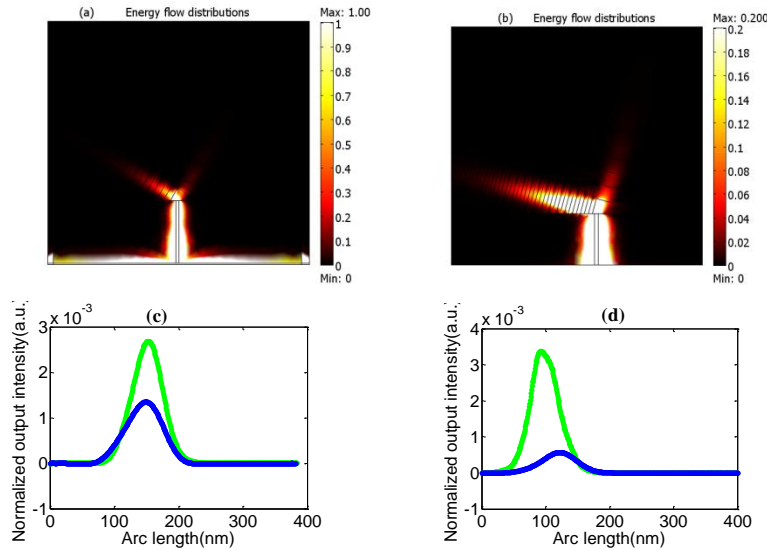
Fig. 1(a) Cross-sectional schematic of the two subwavelength beams splitter; (b)-(e) Energy flow distributions for different θ; (f) is the cross-section views of the output power along one of the two outer surfaces.

Fig 2 shows energy flow distributions for the structure similar with Fig 1(a), but with $\theta_1 \neq \theta_2$. In Fig. 2(a), $\theta_1 = \pi/3$ and $\theta_2 = \pi/6$; in Fig. 2(b), $\theta_1 = 5\pi/12$ and $\theta_2 = \pi/12$. Both of the splitting angles are $\pi/2$. Compared with the previous the uniform beams splitter, the structure with asymmetry can produce two non-uniform beams. Figs. 2(c) and (d) show the cross-section views of the output power along both of the two outer surfaces corresponding to Figs. 2(a) and (b), respectively. The distance between the outer surface and the slit of the Cr film is 380nm. The blue lines represent the output power along of the right outer surfaces, and the green lines represent the right outer surfaces. In Fig. 2(c), the FWHMs are about 53nm and 65nm, for the left outer surface and the right one, respectively. The splitting ratio is about 2 (the splitting ratio is defined as the ratio between the maximum of the output power along the left outer surface and the right outer surface). In Fig. 2(d), the FWHMs are about 52 nm and 63nm, for the left outer surface and the right one, respectively. The splitting ratio is about 5.9. So these asymmetries combined metallodielectric films provide a method to split two subwavelength non-uniform beams with various splitting ratio.

Figs. 2 (a) and (b) Energy flow distributions for $\theta_1 = \pi/3$ and $\theta_2 = \pi/6$, $\theta_1 = 5\pi/12$ and $\theta_2 = \pi/12$; (c) and (d) is the cross-section views of the output power along the two outer surfaces for (a) and (b). The blue lines represent the output power along of the right outer surfaces, and green lines represent the left outer surfaces.

When we combine three or more metallodielectric films, the structure can be used to produce and split subwavelength multi-beams. As shown in Fig. 3(a), the structure is composed of three identical metallodielectric films and $\alpha_1 = \alpha_2 = \alpha_3 = \pi/3$. Energy flow distributions show that the three beams are split, and after propagating 380nm, the FMWHs of the three beams are 56nm, although their intensities are different. The intensity of the middle beam is larger than the other two. In a similar way, the combined metallodielectric films with identical α, which are composed of four metallodielectric films, five metallodielectric films and six metallodielectric films, can split four, five and six subwavelength beams, respectively, shown as the Figs. 3(b)-(e). In Fig. 3(f), it is found that the FMWHs of the above mentioned splitters are about 49nm, 53nm, and 53nm, respectively. For the multi-beams splitters, the intensities of the middle beams are always larger than the marginal ones.
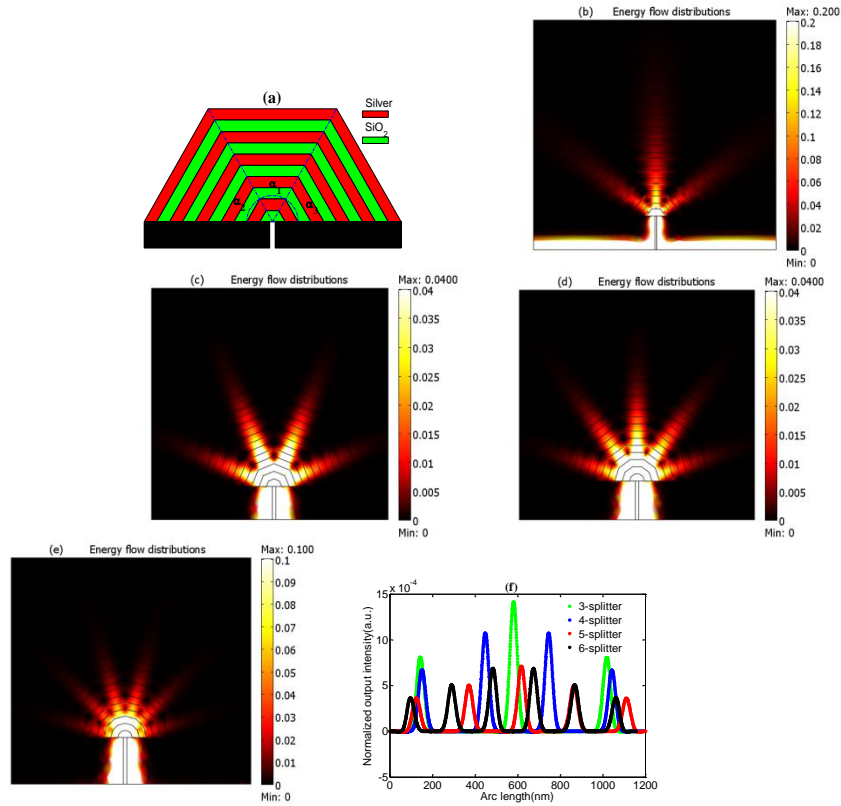

Fig. 3(a) Cross-sectional schematic of the three subwavelength beams splitter; (b)-(e) Energy flow distributions for the three beams splitter, the four beams splitter, the five beams splitters and the six beams splitters; (f) is the cross-section views of the output power along the two outer surfaces of the multi-beams splitters corresponding to (b)-(e)

Next we design the reflected-beams splitters with three metallodielectric films. In Fig. 4(a) and (b), α_1, α_2 and α_3 are both $\pi/3$. The Cr film is above the middle metallodielectric films for Fig. 4(a); and above the left metallodielectric films for Fig. 4(b). The incident beams excited by the slits in Cr film

4

propagate down along the middle metallodielectric film for Fig. 4(a); and down along the left metallodielectric film for Fig. 4(b). In Fig. 4(c), the two reflected beams propagate up left and right uniformly, and the resolutions of them keep 52nm after propagating 380nm. In Fig. 4(c), the two reflected beams propagate up middle and right non-uniformly, and the resolutions of them keep 52nm and 56nm after propagating 380nm, respectively.
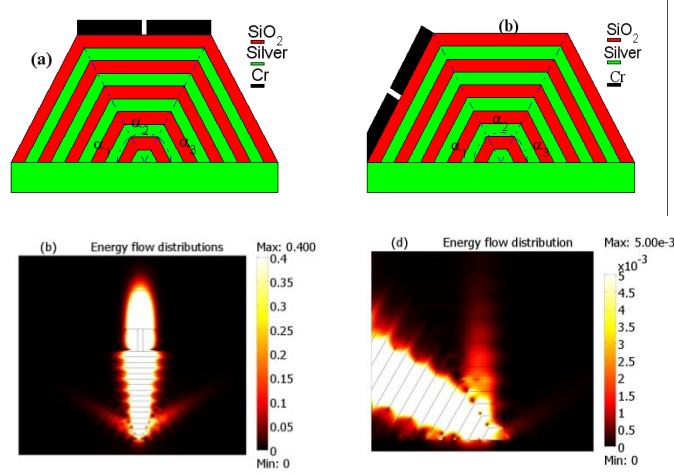

Fig. 4(a) and (b) Cross-sectional schematics of the reflected-beams splitter with the three combined metallodielectric films; (c) and (d) Energy flow distributions for the reflected-beams splitters (a) and (b), respectively.

2.2 Binary zone plate plasminic lens

We proposed a new binary zone plate (BZP) to approximate the bandlimited angular spectrum of a dipole convergent wave. Compared to a Fresnel zone plate, this new zone plate is suitable for bending both radiation waves and radiationless waves to the focus region. With distance $z_0 = 500$ nm, our experiment demonstrated that a focus spot achieved is 300 nm in full width at half maximum (FWHM) with incident wavelength 632.8 nm. In a near field at distance 100 nm, our COMSOL simulation predicted a 193nm-sized focus spot with a considerably large DoF up to 800 nm under illumination of a radially polarized incident wave.

Let's consider a dipole source and its radiated field. A dipole field, radiated from a dipole at the origin, can be expressed as an angular spectrum of plane waves in the form,

$$E(k_x, k_y; z) = \varepsilon \left(\frac{1}{2\pi}\right)^2 \iint_{k_x^2 + k_y^2 \leq k^2} \exp\left(i(k_x x + k_y y)\right) \exp\left(i\sqrt{k^2 - k_x^2 - k_y^2}|z|\right) dk_x dk_y +$$

$$\varepsilon \left(\frac{1}{2\pi}\right)^2 \iint_{k_x^2 + k_y^2 > k^2} \exp\left(i(k_x x + k_y y)\right) \exp\left(-\sqrt{k_x^2 + k_y^2 - k^2}|z|\right) dk_x dk_y, \tag{1}$$

where ε=+1 if z>0 and ε=+1 if z<0. It is denoted $\begin{cases} \sqrt{k^2 - k_x^2 - k_y^2} & \text{if } k_x^2 + k_y^2 \leq k^2 \\ i\sqrt{k_x^2 + k_y^2 - k^2} & \text{if } k_x^2 + k_y^2 > k^2 \end{cases}$, $k = 2\pi/\lambda$. As

illustrated in Fig. 5(a), a dipole field at the aperture (z=0), radiated from a dipole at distance z_0, is read as

$$E(k_x, k_y; z) = -\left(\frac{1}{2\pi}\right)^2 \iint_{k_x^2 + k_y^2 \leq k^2} \exp\left(i(k_x x + k_y y)\right) \exp\left(i\sqrt{k^2 - k_x^2 - k_y^2}\,|z_0|\right) dk_x dk_y +$$

$$-\left(\frac{1}{2\pi}\right)^2 \iint_{k_x^2 + k_y^2 > k^2} \exp\left(i(k_x x + k_y y)\right) \exp\left(-\sqrt{k_x^2 + k_y^2 - k^2}\,|z_0|\right) dk_x dk_y$$

Following Weyl's expansion, this dipole wave-field is equivalent to a convergent spherical wave towards the same distance z_0 in the form,

$$-\frac{1}{2\pi}\frac{\partial}{\partial z}\left(\frac{\exp(-ikr)}{r}\right) = -\left(\frac{1}{2\pi}\right)^2 \iint \exp\left(i(k_x x + k_y y + k_z |z_0|)\right) dk_x dk . \tag{2}$$

$r = \sqrt{x^2 + y^2 + z_0^2}$ and k_z is the same as in Eqn. (1). The denotation of a convergent wave-field follows that of an incoming wave-field, as in Ref. 12. According to the reciprocal approach, the convergent dipole field at the aperture, $-\frac{1}{2\pi}\frac{\partial}{\partial z}\left(\frac{\exp(-ikr)}{r}\right)$, enables to be convergent towards a focus spot at the same distance z_0, as illustrated in Fig. 8(b). The subwavelength structure at the aperture is to approximate a spherical wave-field having a bandlimited angular spectrum of plane waves.
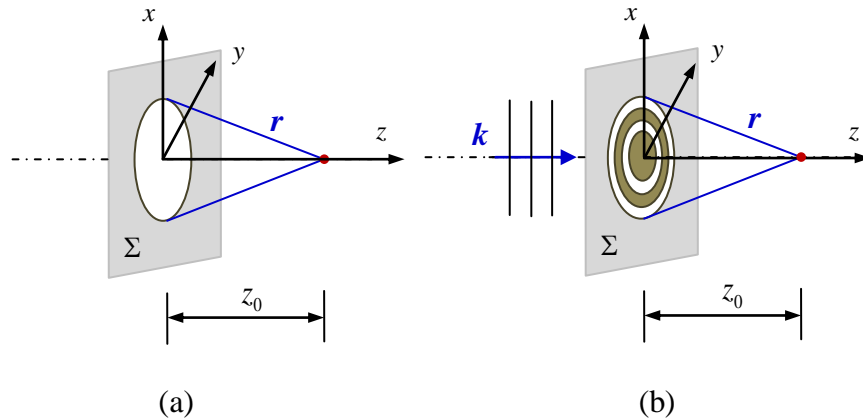

(a)   (b)

Fig. 5 (a) Schematic of a convergent dipole wave at the aperture plane Σ (z = 0), radiated from a dipole located at z = z_0. The wave field is denoted as $\frac{-1}{2\pi}\frac{\partial}{\partial z}\frac{e^{-ik|r|}}{|r|}$, $r = \sqrt{x^2 + y^2 + z_0^2}$ and k =2π/λ. According to the reciprocal approach, both radiation waves and radiationless waves in the field can still be convergent onto the focus spot at the same distance z_0 as the dipole source. (b) Zone plate structure at the aperture is incident with a p-polarized plane wave to approximate a convergent dipole wavefront.

The zone plate structure has been fabricated in gold thin film having the measured thickness of 130 nm, supported on a quartz substrate. The focused ion beam based on AURIGA crossbeam (FIB-SEM) workstation from Carl Zeiss was used. The fabrication parameters include: Ga+ ion energy 30 keV, incident angle 0°, beam current 10 pA, beam overlap 50% in both horizontal and vertical directions. With a p-polarized incident plane wave with its electric field component parallel to the x direction, the near electric field is measured by a nearfield scanning optical microscope (NTEGRA NSOM of NT-MDT). The incident wavelength is 632.8 nm.
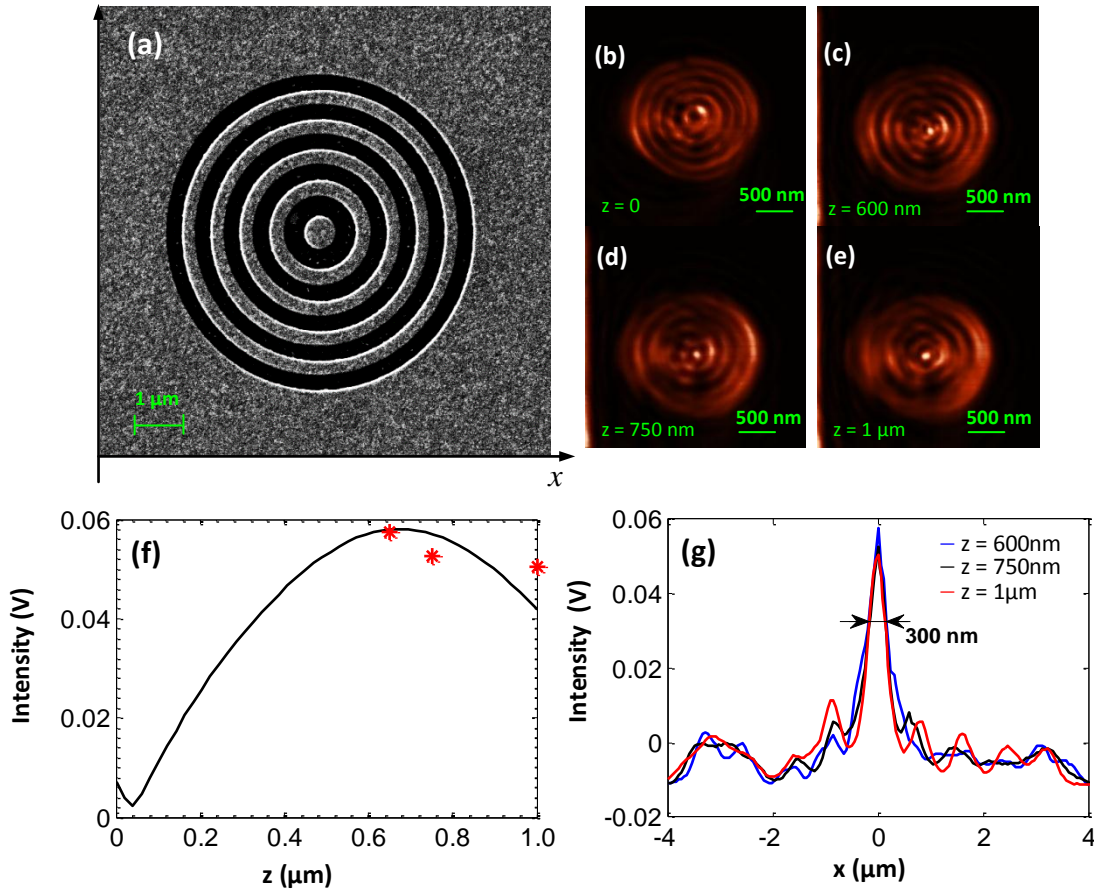

Fig. 6 (a) The SEM picture of a BZP plasmonic lens, fabricated by focused ion beam in gold thin film (thickness, 130 nm). The lens was designed for f_d = 500 nm and λ_{in} = 632.8 nm. The experimental electric field data in the x-y plane were measured at different longitudinal distances (b)-(e) z = 0, 600 nm, 750 nm, and 1 μm. A small focus spot was observed at 600 nm and even at a distance up to 1 μm. (f) Actual electric field intensity along the z direction and (g) the beam profile at different distances.

Fig. 6 shows the main experimental results. The SEM image of a fabricated plasmonic lens is shown in Fig. 6(a). Its optical properties were measured in the x-y plane along different longitudinal distances as shown in Figs. 6(b)-4(e). Significant subwavelength focusing is observed at the distance of 600 nm and even at 6(f). On the focal plane, significant focal spot achieved is 300±25 nm in FWHM, adequately

smaller than the diffraction limit. In addition the focal spot size achieved in a far field is 350 nm at z = 750 nm and smaller than 400 nm at z = 1 μm.

With actual thin film thickness of 130 nm, the results of NSOM measurement are in agreement with those of COMSOL simulation. Also, depth of focus in the experiment was observed from 600 nm to 1 μm, equivalent to $\pm\left(\Delta r_{\text{outermost}}/\lambda\right)^2 = \pm 0.257\,\mu m$. In the figure, the simulated field distribution along the z direction is normalized to the actual values at distance 600 nm.

In addition, the surface topography forms in the process of Ga+-ion-beam bombardments during the process of material removal and redeposition as well. The surface topography can be described as a "V"-shape model or a more feasible U-shape model. As surface waves are propagated along the fabricated surface boundary and the diffraction of surface waves occurs at corners, the change in surface topography can produce considerably changes in the optical field.

2.3 Low-loss on-chip integrated plasmonic waveguide

We experimentally achieved a robust silicon-based plasmonic waveguide structure that can confine both E_x- and E_y-polarized SPP modes and exhibit propagation loss as low as 0.2dB/μm with coupling efficiency of ~50%, which is the lowest reported, to the best of our knowledge.

Fig. 7 shows the simple yet robust plasmonic waveguide (PWG) structure consisting of a silicon waveguide coated by thin metal film. The proposed PWG structure consists of narrow silicon waveguide clad by gold film without top dielectric spacer layer and with metal thickness much smaller than those demonstrated earlier.
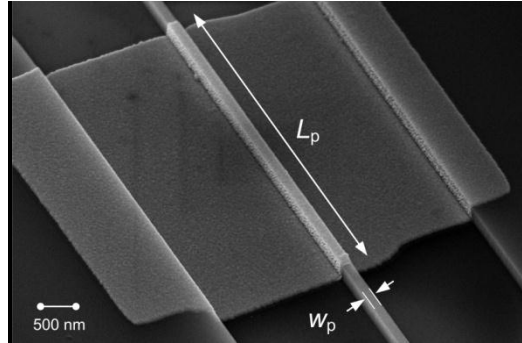

Fig. 7. SEM micrograph of SOIPWG before ZEP coating.

The modal effective indices (n_{eff}) of SOI waveguide (SOIWG) and the proposed PWG (SOIPWG) as a function of waveguide width (W_P) are presented in Fig. 8, where the mode analysis is carried out by Finite Element Method (FEM). One can see that a thin metal is sufficient to confine both quasi-TE (E_x-polarized) and quasi-TM (E_y-polarized) SPP modes.

The dependence of modal effective index on waveguide width is similar to the case of conventional dielectric waveguide, except for the fundamental quasi-TE mode (quasi-TE$_0$) where the effective index

decreases at increasing width. This is because quasi-TE$_0$ mode originates from two interacting E_x-polarized SPP modes at two waveguide sidewalls. At increasing waveguide width, the coupling strength between these modes decreases and the optical intensity is increasingly more localized at interfaces, resulting in lower effective index. In comparison with TE mode of a typical SOI waveguide (solid line), there is a large index mismatch between the SOIPWG and SOIWG modes, indicating that the coupling efficiency between SOIWG and SOIPWG will always be limited by Fresnel reflection caused by mode index mismatch [$R=(n_{\mathrm{eff,2}}-n_{\mathrm{eff,1}})^2/(n_{\mathrm{eff,2}}+n_{\mathrm{eff,1}})^2$]. More importantly, this remains the case regardless of whether taper structure is employed during coupling or whether there is a total overlap between the mode profiles of SOIWG and PWG. By substituting the effective index for SOIPWG ($n_{\mathrm{eff}}\sim 3.1$) and SOIWG ($n_{\mathrm{eff}}\sim 2.3$) modes at W_{p}=450nm, the maximum coupling efficiency can be estimated as ~0.1dB/facet.
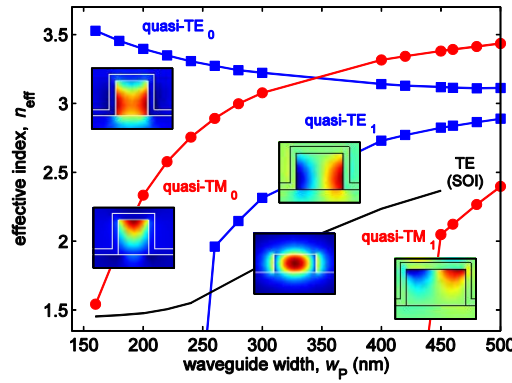

Fig. 8. Mode characteristics of quasi-TE and quasi-TM modes of SOIPWG for t_{Au}=40nm gold thickness. The TE mode of SOIWG is also shown for comparison. The insets show the electric field profiles corresponding to each mode.

The device fabrication is in the following steps. First, the SOI photonic waveguides were fabricated by 193nm DUV Lithography, where the waveguide thickness is 220nm and the lower oxide cladding is 2μm. The device consists of main waveguide (of waveguide width W_{SOI}=450nm) tapered down at the middle section to narrow waveguide which has waveguide width (W_{P}) ranging from 150nm to 250nm. The taper length is L_{t}=10μm, while the narrow waveguide length (L_{N}) varies from 50μm to 400μm. The focused grating couplers were integrated at both sides as input and output ports, which are 1mm apart and designed to excite TE mode in SOI waveguide. Second, the SOIWG was then converted to SOIPWG by covering the middle section of the narrow silicon waveguide with gold film at a length of L_{P}, which is fixed at 10% of the total narrow waveguide length, i.e., L_{P}=0.1L_{N}. In this step electron beam lithography was employed to make opening before metal deposition, and 5kV acceleration voltage was chosen to ensure the electron beam penetration depth not exceeding the resist thickness so as to prevent substrate damage. Then, the metal deposition was carried out by e-beam evaporation, where 3nm thick titanium was used as adhesion layer before 40nm gold deposition took place. Finally, the samples were spun coated with ZEP520 e-beam resist for isolation. Here, the e-beam resist was preferred to conventional photoresist due to the lower optical absorption. The SEM micrograph of gold coated SOI waveguide before ZEP coating is shown in Fig. 7.

For device measurements, the light is coupled and collected by means of near-vertical coupling mechanism, where the light source and detector used in this work is SANTEC TLS-510 tunable laser

and ILX FPM-8210 fiber power meter, respectively. The measurements were carried out before and after metal deposition in order to extract SPP related losses. Here, the fundamental TE mode of SOIWG can only couple to quasi-TE_0 mode in SOIPWG due to different symmetry conditions of quasi-TM_0, which has anti-symmetric E_x profiles. The same reasoning applies for the higher order plasmonic modes, i.e., quasi-TE_1 and quasi-TM_1. The normalized transmission of SOIPWG for different widths (W_p) and lengths (L_p) are presented in Fig. 9(a). Each point corresponds to measurements across 6 samples with standard deviation represented by the error bar. The extraction of both the propagation (α_{SPP}, α_{SOI}) and coupling (η_{SPP}, η_{SOI}) losses are obtained from linear fit, and shown in Fig. 9(b) as a function of W_P. The exponential dependence of α_{SOI} on W_P is related to the mode cut-off condition, i.e., the width below which the light is no longer confined in the waveguide. FEM simulations show that the cut-off width of ZEP520 coated SOIWG is 200nm, which corresponds experimentally to ~60dB/cm propagation loss in Fig. 9(b).
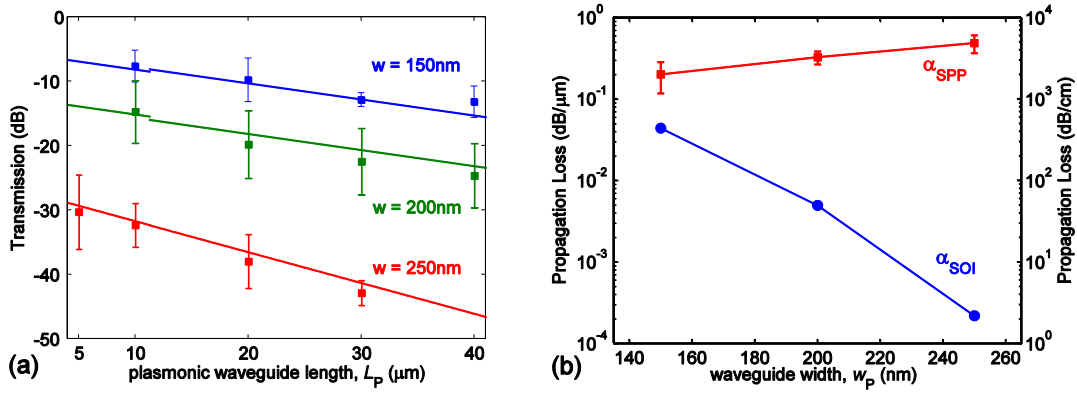

Fig. 9. (a) Loss characteristics of SOIPWG, and (b) deduced propagation losses of SOIPWG and SOIWG for different widths at λ=1550nm.

On the other hand, the measured propagation losses for SOIPWG are α_{SPP}=0.2±0.08dB/μm (W_P=150nm), α_{SPP}=0.32±0.06dB/μm (W_P=200nm), and α_{SPP}=0.48±0.12dB/μm (W_P=250nm). The observed trend where α_{SPP} increases with W_P is rather unusual, particularly when numerical simulations normally show decreasing trend of propagation loss at increasing waveguide width. We believe this can be attributed to material absorption of titanium adhesion layer, which is known to have large extinction coefficient in infrared wavelength range. Since SPP mode shifts towards the sidewalls at increasing W_P, the field overlap of SPP mode with titanium layer is also expected to increase. In addition to this, surface scattering loss will also increase due to increased interaction with gold film roughness. The total insertion loss of SOIPWG consists of (1) the coupling loss at the grating couplers ($\eta_{grating}$), (2) the coupling loss due to transition from main waveguide to narrow SOIWG (η_{SOI}), and (3) the coupling loss at SOIWG-SOIPWG interfaces (η_{SPP}). Fig. 10 shows the coupling losses for both coated (η_{SOI}+η_{SPP}) and uncoated (η_{SOI}) waveguides. Here, the coupling losses have been normalized by grating coupler loss, which is measured as $\eta_{grating}$~4dB/facet. The decrease of η_{SOI} with W_P is as expected due to increasing sidewall scattering loss resulting from the increase of optical mode field size in smaller W_P. The coupling loss between SOIWG and SOIPWG (η_{SPP}) can then be deduced by subtracting the total coupling loss of coated and uncoated waveguides, as denoted by dashed line.

The measured η_{SPP} increases with W_P, which increases from η_{SPP}~2.91dB/facet (W_P=150nm) to η_{SPP}~13dB/facet (W_P=250nm). Since SOIWG couples directly to SOIPWG in all our experiments (as

10

shown by the inset of Fig. 10), we believe there is cavity effect formed by mode index differences between SOIWG and SOIPWG modes (see Fig. 9). This is well supported by our FEM simulations, where a slight change of L_P could lead to intensity buildup within SOIPWG region and results in either full-transmission (resonance) or full-reflection (anti-resonance). It is therefore possible that the coupling loss appears large when it is far from resonance condition. For this reason, the measured coupling losses for W_P=200nm and W_P=250nm may not be accurate as they are convoluted by such cavity effects. Furthermore, FEM simulations show the estimated coupling loss of ~2dB/facet for 150nm$\leq W_P \leq$250nm, about the same order as our experimentally measured η_{SPP}=2.91±1.57dB/facet for W_P=150nm. By calculating loss due to Fresnel reflection for W_P=150nm (~84%), the field overlap between SOIWG and SOIPWG can be estimated as ~60%, in agreement with numerical simulations.
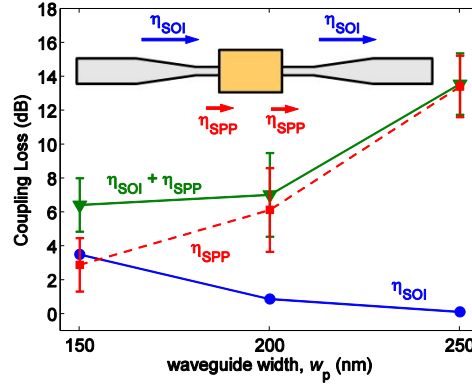

Fig. 10. The coupling losses of SOIWG (η_{SOI}) and SOIPWG (η_{SPP}).

2.4   Dielectric nanocavity metamaterial lens for super resolution imaging in visible range

We proposed a dielectric nanocavity metamaterial lens. Our simulations with the finite-element method indicate that this lens can transfer image to a much longer distance with resolution better than 40 nm and work in visible range. With proper design, it can also magnify image to the size detectable by conventional optical system. We believe that this work will accelerate the advancement of metamaterial lenses.

3. Future work

We have investigated several metal-dielectric structures theoretically and experimentally and explored their applications for beam splitting, super focusing, low loss plasmonic waveguide and new type of metamaterial lens. The results are exciting. In the near future, we will continuously explore new structures made of metal and dielectric and develop new devices and components so as to achieve new generation nanophotonic technologies.

References:

[1].   T. Erqin et al. Science. 1186351, 2010
[2].   X. Zhang et al., Nature Materials, VOL 8, 568, 2009
[3].   E. Betzig, J. K. Trautman, T. D. Harris, J. S. Weiner and R. L. Kosrelak, Science 251, 1468-1470 (1991).
[4].   Z. Jacob, L. V. Alekseyev and E. Narimanov, Optics Express, V14, n18 (2006).
[5].   Z. W. Liu, H. Lee, Y. Xiong, C. Sun, X. Zhang, Science 315, 1686 (2007).
[6].   Changchun Yan, Dao Hua Zhang, Yuan Zhang, Dongdong Li, and M. A. Fiddy, Optics Express 18, 14794, 2010.
[7].   Z. M. Huang, J. Q. Xue, Y. Hou, J.H. Chu and D. H. Zhang, Phys. Rev. B 74, 193105 2006.